Enhanced Campbell Diagram With the Concept of H_∞ in Rotating Machinery: Lee Diagram

Chong-Won Lee[1]
Fellow ASME
e-mail: cwlee@kaist.ac.kr

Yun-Ho Seo
e-mail: yunho@kaist.ac.kr

Department of Mechanical Engineering,
Center for Noise and Vibration Control (NOVIC),
KAIST,
Daejeon 305-701, Korea

The Campbell diagram, a frequency-speed diagram, has been widely used for prediction of possible occurrence of resonances in the phase of design and operation of rotating machinery since its advent in 1920s. In this paper, a set of new frequency-speed diagrams, which is referred to as the Lee diagram, is newly proposed, where the conventional Campbell diagram is incorporated with the concept of the infinity norm of directional frequency response matrix (dFRM) associated with a rotor with rotating and stationary asymmetry in general. The dFRM is constructed based on complete modal analysis of a linear periodically time-varying rotor model formulated in the complex coordinates. It is shown that the Lee diagram is powerful in that it can identify the modes of symmetry, rotating and stationary asymmetry, and extract only a few critical resonances out of the, otherwise, overcrowded ones without a measure of priority as in the Campbell diagram. In order to demonstrate the power of the Lee diagram in design and operation of rotating machines, three examples are treated: a typical anisotropic rigid rotor, a simple general rotor, and a two-pole generator. [DOI: 10.1115/1.3173610]

Keywords: modal strength, norm order of eigenvectors, Campbell diagram, Lee diagram, strong and weak modes, infinity norm of directional frequency response functions, periodically time-varying system

1 Introduction

In this introductory section, we state briefly the state of the art in modal analysis of linear rotor-bearing systems, analyze the nature of the whirl speed chart (better known as the Campbell diagram), which is the plot of the modal frequencies and possible excitation order lines against the rotational speed, and discuss previous attempts to improve the diagram.

1.1 State of the Art in Modal Analysis of Rotor-Bearing System. In general, a rotor-bearing system has two main parts, rotor and stator. According to the nonaxisymmetric properties of the rotor and stator parts, a rotor-bearing system may be classified into four types [1,2]: *isotropic* (symmetric) rotor system, when both the rotor and the stator are axisymmetric; *anisotropic* rotor system, when the rotor is axisymmetric but the stator is not (stationary asymmetry); *asymmetric* rotor system when the stator is axisymmetric but the rotor is not (rotating asymmetry); and *general* rotor when neither the rotor nor the stator is axisymmetric (both stationary and rotating asymmetry). Modal analysis of the isotropic [3], anisotropic [3–5], and asymmetric linear rotor systems [2], which are essentially formulated as a time-invariant linear system, has been well developed and the commercial finite element method (FEM) codes, such as NASTRAN, ANSYS, SAMCEF, etc., have also become available in the market, except for modal analysis of the general rotor system. On the other hand, the modal analysis of general rotor systems, which is characterized by the presence of periodically time-varying parameters, has recently been conducted using both the Floquet theory [6] and the modulation coordinate technique [7].

1.2 Campbell Diagram. Rotating machines nowadays are designed such that they can be safely operated beyond or passing through many critical speeds. Rotating machinery consists of many structural elements such as shaft, disk, blade, bearing/seal/damper, casing, and foundation. Not only each machine structure reveals its own local dynamic characteristics, but the whole machine as an assemblage of part structures also reveals global dynamic characteristics. The dynamic properties of most common interest in rotating machinery typically include the critical speeds, stability of modes, and forced response. The critical speeds of a rotor are defined as the rotational speeds at which the speed-dependent modal (natural) frequencies, rigid or flexible, intersect with the order lines associated with possible excitation sources of paramount interest. Perhaps one of the most convenient and elegant graphical presentations for predicting critical speeds is known as the Campbell diagram, which was introduced by Campbell in 1924 in a study of circumferential waves in turbine disks [8,9]. He believed that "one of the most important features in the design and manufacture of a steam turbine is the elimination of the possibility of vibration occurrence at the various natural frequencies of its disk wheels and buckets." It is often referred to as the whirl speed chart (map) [10], frequency-speed diagram, natural frequency-speed map, damped natural frequency map, interference map, and frequency interference diagram, where the whirl speeds, or equivalently the modal frequencies, and the order lines of possible excitation forces are plotted against the rotational speed. The Campbell diagram is helpful for design and practice engineers to judge on the margin of safe operation in the design as well as field operation processes. The Campbell diagram has been popularly adopted in the design of rotors with bladed disks such as turbines and fans, where the blade natural frequencies and the excitation order lines associated with the blade passing frequency and the integer multiples are easily identified [11,12]. However, its usage is limited in the sense that it does not provide practice engineers with the essential information such as the stability and forced response of the actual rotor system, particularly when the system possesses both stationary and rotating asymmetry. In other words, it does not tell us about which critical speeds have to be considered seriously in design and operation—the severity of the rotor response at each critical speed. For the critical speeds of an

[1]Corresponding author.

Contributed by the Applied Mechanics Division of ASME for publication in the JOURNAL OF APPLIED MECHANICS. Manuscript received March 24, 2008; final manuscript received April 19, 2009; published online December 14, 2009. Review conducted by Wei-Chau Xie.

isotropic rotor system associated with unbalance excitation, the backward whirl speeds are traditionally indicated by broken lines, in order to indicate the less importance of the backward critical speeds in the unbalance response of the isotropic rotor system [13].

1.3 Previous Attempts for Enhanced Campbell Diagram. One method of accommodating the stability information, which has been well adopted by many researchers in the past, is simply to add the information of the modal damping as well as frequency for each mode in the Campbell diagram [14], or to draw root loci with the rotational speed varied. The relative stability of each mode can be addressed based on the added information on modal damping, but as the number of modes increases, the additional information complicates the understanding of the plot, obscuring the essence of information.

Forced responses, including the most common unbalance responses, of a rotor at critical speeds essentially tell us about what actually happens with the rotor in operation subject to known excitation forces. However, the forced responses never represent the real rotor characteristics, unless the accurate quantitative information of all excitation forces, say the precise unbalance distribution, is available, which is an impractical, if not impossible, requirement.

Fortunately, the rotordynamic modeling and analysis have been quite successful in the past, since the rotordynamic modeling based on the finite element method or transfer matrix method (TMM) is relatively simple in nature compared with other complicated structures and the parameter uncertainties are rarely encountered. From the rotordynamic analysis, we can obtain useful modal information such as the modal damping and frequency, and, above all, the modal vector. Based on the modal information, we can simulate forced response for excitation forces given. Often we assume the nature of excitation forces and freely simulate all probable situations. However, the forced response varies as the excitation force is changed. It means that, unless the exact information of excitation force is given, the forced response represents one realization of innumerable situations encountered in practice.

As the rotor system configuration becomes complicated as in the case of bladed turbine wheels, the corresponding whirl speed charts are overcrowded with the many subsystem natural frequencies and order lines, resulting in many intersections. However, not all the intersections may be engaged with possible resonances, when each order line is associated with a particular mode. Singh [15] successfully introduced a method of reducing the number of meaningful intersections by using the relation between the order lines and the mode shapes of bladed turbine wheels. However, his method still lacks the information of modal damping and eigenvectors in predicting the critical speeds.

1.4 Proposition of a New Whirl Speed Chart. Modal damping certainly has to do with the relative stability of mode. Presence of modes with positive damping at a rotational speed indicates the unstable free response of the rotor at that speed, the response becoming large as far as the linearity assumption allows. Modes of light damping contribute more to the transient response than modes of heavy damping. However, it is not completely correct to say that modes of light damping contribute more to the steady-state response than modes of heavy damping. In fact, the magnification factor near the modal frequency for the harmonic response is inversely proportional to modal damping, but the response is also proportional to the residue that is a product of the modal and adjoint vectors as well as the force itself. Thus, the modal vector, whose importance is often forgotten, should be accounted whenever the severity of the response is addressed [16]. Based on the modal analysis of general rotor systems, the rigorous norm analysis of modal vectors has recently been carried out [17], in order to represent the strength of modes in the complex coordinate system. In this paper, a new method of reflecting the importance of each mode in the Campbell diagram is proposed by calculating the infinity norms of the four directional frequency response matrices [3] defined in the complex coordinates, which are referred to as the Lee diagram [18]. The Lee diagram is a function of the frequency and the rotational speed, which can be used as a powerful and effective tool in selecting only a few important possible resonances for design and operation of rotors in practice, from otherwise too many possible ones.

2 Complex Modal Analysis of General Rotor Systems

In this section, we briefly summarize the modal analysis method for a general rotor system with both the rotating and the stationary asymmetry described in Ref. [6] and the concept of modal strength developed in Ref. [17].

2.1 Modal Analysis Using Floquet Theory [6]. For a general rotor system with rotating and stationary asymmetry, the equation of motion can be conveniently written in the complex stationary coordinates, as follows [3,19–21]:

$$\mathbf{M}_\mathbf{f}\ddot{\mathbf{p}}(t) + \mathbf{C}_\mathbf{f}\dot{\mathbf{p}}(t) + \mathbf{K}_\mathbf{f}\mathbf{p}(t) + \{\mathbf{M}_\mathbf{b}\ddot{\bar{\mathbf{p}}}(t) + \mathbf{C}_\mathbf{b}\dot{\bar{\mathbf{p}}}(t) + \mathbf{K}_\mathbf{b}\bar{\mathbf{p}}(t)\} + e^{j2\Omega t}\{\mathbf{M}_\mathbf{r}\ddot{\bar{\mathbf{p}}}(t) + \mathbf{C}_\mathbf{r}\dot{\bar{\mathbf{p}}}(t) + \mathbf{K}_\mathbf{r}\bar{\mathbf{p}}(t)\} = \mathbf{g}(t) \quad (1)$$

Here, the $N\times 1$ complex response and force vectors, $\mathbf{p}(t)$ and $\mathbf{g}(t)$, defined by the real response vectors, $\mathbf{y}(t)$ and $\mathbf{z}(t)$, and the real excitation vectors, $\mathbf{f}_y(t)$ and $\mathbf{f}_z(t)$, respectively, are

$$\mathbf{p}(t) = \mathbf{y}(t) + j\mathbf{z}(t), \quad \bar{\mathbf{p}}(t) = \mathbf{y}(t) - j\mathbf{z}(t), \quad \mathbf{g}(t) = \mathbf{f}_y(t) + j\mathbf{f}_z(t), \quad \bar{\mathbf{g}}(t) = \mathbf{f}_y(t) - j\mathbf{f}_z(t) \quad (2)$$

where j means the imaginary number; N is the dimension of the complex coordinate vector; $\mathbf{g}(t)$ includes the force and moment; Ω is the rotational speed; "-" denotes the complex conjugate; $\mathbf{M}_i$, $\mathbf{C}_i$, and $\mathbf{K}_i$ denote the complex valued $N\times N$ generalized mass, damping, and stiffness matrices, respectively; and the subscripts **f**, and **b** and **r** refer to the mean value, and the deviatoric values for anisotropy (stationary asymmetry) and asymmetry (rotating asymmetry), respectively. For an isotropic rotor, $\mathbf{M_b}=\mathbf{C_b}=\mathbf{K_b}=\mathbf{M_r}=\mathbf{C_r}=\mathbf{K_r}=\mathbf{0}$; for an anisotropic rotor, $\mathbf{M_r}=\mathbf{C_r}=\mathbf{K_r}=\mathbf{0}$; and for an asymmetric rotor, $\mathbf{M_b}=\mathbf{C_b}=\mathbf{K_b}=\mathbf{0}$. The terms, which are preceded by $e^{j2\Omega t}$ inherently appear in Eq. (1) when both rotating and stationary asymmetries exist in the system. Note here that Eq. (1) represents the periodically time-varying linear rotor system with the period $T=\pi/\Omega$, when it runs at a constant rotational speed Ω, and that it includes the external and internal damping, gyroscopic moment, and Coriolis effect. When either rotating or stationary asymmetry does not exist, the equation of motion becomes, or it can be easily transformed to, a time-invariant differential equation [7].

In Eq. (1) and its complex conjugate form, the complex equation of motion can be constructed as

$$\mathbf{M}(t)\ddot{\mathbf{q}}(t) + \mathbf{C}(t)\dot{\mathbf{q}}(t) + \mathbf{K}(t)\mathbf{q}(t) = \mathbf{f}(t) \quad (3)$$

where

$$\mathbf{q}(t) = \begin{Bmatrix} \mathbf{p}(t) \\ \bar{\mathbf{p}}(t) \end{Bmatrix}, \quad \mathbf{f}(t) = \begin{Bmatrix} \mathbf{g}(t) \\ \bar{\mathbf{g}}(t) \end{Bmatrix},$$

$$\mathbf{M}(t) = \begin{bmatrix} \mathbf{M_f} & \mathbf{M_b} + \mathbf{M_r}e^{j2\Omega t} \\ \overline{\mathbf{M}_\mathbf{b}} + \overline{\mathbf{M}}_\mathbf{r}e^{-j2\Omega t} & \overline{\mathbf{M}}_\mathbf{f} \end{bmatrix}$$

$$\mathbf{C}(t) = \begin{bmatrix} \mathbf{C_f} & \mathbf{C_b} + \mathbf{C_r}e^{j2\Omega t} \\ \overline{\mathbf{C}}_\mathbf{b} + \overline{\mathbf{C}}_\mathbf{r}e^{-j2\Omega t} & \overline{\mathbf{C}}_\mathbf{f} \end{bmatrix},$$

$$\mathbf{K}(t) = \begin{bmatrix} \mathbf{K_f} & \mathbf{K_b} + \mathbf{K_r}e^{j2\Omega t} \\ \overline{\mathbf{K}}_\mathbf{b} + \overline{\mathbf{K}}_\mathbf{r}e^{-j2\Omega t} & \overline{\mathbf{K}}_\mathbf{f} \end{bmatrix} \quad (4)$$

Equation (3) can be rewritten in the state space form as

$$\mathbf{A}(t)\dot{\mathbf{w}}(t) = \mathbf{B}(t)\mathbf{w}(t) + \mathbf{F}(t) \tag{5}$$

where

$$\mathbf{A}(t) = \begin{bmatrix} \mathbf{0} & \mathbf{M}(t) \\ \mathbf{M}(t) & \mathbf{C}(t) \end{bmatrix}, \quad \mathbf{B}(t) = \begin{bmatrix} \mathbf{M}(t) & \mathbf{0} \\ \mathbf{0} & -\mathbf{K}(t) \end{bmatrix},$$

$$\mathbf{w}(t) = \begin{Bmatrix} \dot{\mathbf{q}}(t) \\ \mathbf{q}(t) \end{Bmatrix}, \quad \mathbf{F}(t) = \begin{Bmatrix} \mathbf{0} \\ \mathbf{f}(t) \end{Bmatrix} \tag{6}$$

The adjoint equation can be derived, introducing the adjoint state vector $z(t)$, from the homogeneous part of Eq. (5) as follows [22,23]:

$$\dot{z}(t) = -[\overline{\mathbf{A}}^{-1}(t)\overline{\mathbf{B}}(t)]^T z(t) \tag{7}$$

Utilizing the Floquet theory, we can now construct the eigenvalue problem for this periodically time-varying system with the period $T = \pi/\Omega$ as follows:

$$\mathbf{A}(t)\dot{\mathbf{r}}(t) + \mu\mathbf{A}(t)\mathbf{r}(t) = \mathbf{B}(t)\mathbf{r}(t) \tag{8a}$$

$$\mu \boldsymbol{l}^T(t)\mathbf{A}(t) - \boldsymbol{l}^T(t)\dot{\mathbf{A}}(t) - \dot{\boldsymbol{l}}^T(t)\mathbf{A}(t) = \boldsymbol{l}^T(t)\mathbf{B}(t) \tag{8b}$$

with the bi-orthonormality conditions [23]

$$\boldsymbol{l}_s^{kT}(t)\mathbf{A}(t)\mathbf{r}_r^i(t) = \delta_{rs}^{ik}, \quad r,s = \pm 1, \pm 2, \ldots, \pm N; \quad i,k = B,F \tag{9a}$$

$$\dot{\boldsymbol{l}}_s^{kT}(t)\mathbf{A}(t)\mathbf{r}_r^i(t) + \boldsymbol{l}_s^{kT}(t)\dot{\mathbf{A}}(t)\mathbf{r}_r^i(t) - \boldsymbol{l}_s^{kT}(t)\mathbf{B}(t)\mathbf{r}_r^i(t) = \mu_r^i \delta_{rs}^{ik} \tag{9b}$$

where μ, which are termed Poincare exponents, and $\mathbf{r}(t)$ and $\boldsymbol{l}(t)$, which are periodic vectors of period $T = \pi/\Omega$, are equivalent to the eigenvalues, and right and left eigenvectors for time-invariant systems. Here, the superscript T means the transpose and δ_{rs}^{ik} is the Kronecker delta defined as

$$\delta_{rs}^{ik} = \begin{cases} 1 & \text{for } i = k \quad \text{and} \quad r = s \\ 0 & \text{otherwise} \end{cases}$$

The superscripts B and F refer to the backward and forward modes, respectively, following the well-established convention for mode classification in rotor dynamics [3] and the subscripts r and s with the positive and negative integers are used to identify the original (strong) and its complex conjugate (weak) modes, respectively [3,17].

Substituting the relation $\mathbf{w}(t) = \{\dot{\mathbf{q}}(t) \quad \mathbf{q}(t)\}^T = \mathbf{r}(t)\eta(t)$ with $\mathbf{q}(t) = \mathbf{u}_\mathbf{c}(t)\eta(t)$ and Eq. (8a) into the homogeneous part of Eq. (5), we obtain the relation given by

$$\mathbf{r}(t) = \begin{Bmatrix} \dot{\mathbf{u}}_\mathbf{c}(t) + \mu\, \mathbf{u}_\mathbf{c}(t) \\ \mathbf{u}_\mathbf{c}(t) \end{Bmatrix} \tag{10}$$

Likewise, substituting the relation $\mathbf{z}(t) = \overline{\mathbf{A}}^T(t)\bar{\boldsymbol{l}}(t)\zeta(t)$ and Eq. (8b) into the adjoint Eq. (7), we obtain the relation given by

$$\boldsymbol{l}(t) = \begin{Bmatrix} -\dot{\bar{\mathbf{v}}}_\mathbf{c}(t) + \{\mu - [\dot{\mathbf{M}}(t)\mathbf{M}^{-1}(t)]^T\}\bar{\mathbf{v}}_\mathbf{c}(t) \\ \bar{\mathbf{v}}_\mathbf{c}(t) \end{Bmatrix} \tag{11}$$

Here, the T periodic modal and the adjoint vectors are composed, respectively, of

$$\mathbf{u}_\mathbf{c}(t) = \begin{Bmatrix} \mathbf{u}(t) \\ \hat{\mathbf{u}}(t) \end{Bmatrix}, \quad \mathbf{v}_\mathbf{c}(t) = \begin{Bmatrix} \mathbf{v}(t) \\ \hat{\mathbf{v}}(t) \end{Bmatrix} \tag{12}$$

The complex state and adjoint vectors, $\mathbf{w}(t)$ and $z(t)$, can be expanded in terms of the T periodic eigenvectors and the adjoint vectors, respectively, for the rotor system (5), as

$$\mathbf{w}(t) = \sum_{r=1}^{4N} \{\mathbf{r}(t)\eta(t)\}_r = \sum_{i=B,F} \sum_{r=-N}^{N}{}' \{\mathbf{r}(t)\eta(t)\}_r^i \tag{13a}$$

$$\mathbf{z}(t) = \sum_{r=1}^{4N} \{\bar{\mathbf{l}}(t)\zeta(t)\}_r = \sum_{i=B,F} \sum_{r=-N}^{N}{}' \{\bar{\mathbf{l}}(t)\zeta(t)\}_r^i \tag{13b}$$

where the prime notation in the summation implies exclusion of $r=0$, $\eta(t)$, and $\zeta(t)$ are the principal coordinates of the original and adjoint systems, respectively.

Substituting Eq. (13a) into Eq. (5), using the relation (8a), premultiplying by $\boldsymbol{l}_s^{kT}$, and using the bi-orthonormality condition (9a) and the relation (11), we obtain the $4N$ sets of complex modal equations of motion as

$$\dot{\eta}_r^i(t) = \mu_r^i \eta_r^i(t) + \bar{\mathbf{v}}_{\mathbf{c}r}^{iT}(t)\mathbf{f}(t) = \mu_r^i \eta_r^i(t) + \bar{\mathbf{v}}_r^{iT}(t)\mathbf{g}(t) + \bar{\hat{\mathbf{v}}}_r^{iT}(t)\bar{\mathbf{g}}(t),$$

$$r = \pm 1, \pm 2, \ldots, \pm N, \quad i = B,F \tag{14}$$

Recalling the Floquet theory that, from the one periodic solution, the entire time response of the eigensolutions can be expressed periodically with the base of that period, we can expand the T periodic modal vector $\mathbf{u}_\mathbf{c}(t)$ and the adjoint vector $\mathbf{v}_\mathbf{c}(t)$ in Eq. (12) by Fourier series as follows [6]:

$$\mathbf{u}_r^i(t) = \sum_{m=-\infty}^{\infty} \mathbf{u}_{r(m)}^i e^{j2m\Omega t}, \quad \hat{\mathbf{u}}_r^i(t) = \sum_{m=-\infty}^{\infty} \hat{\mathbf{u}}_{r(m)}^i e^{j2m\Omega t} \tag{15a}$$

$$\mathbf{v}_r^i(t) = \sum_{m=-\infty}^{\infty} \mathbf{v}_{r(m)}^i e^{j2m\Omega t}, \quad \hat{\mathbf{v}}_r^i(t) = \sum_{m=-\infty}^{\infty} \hat{\mathbf{v}}_{r(m)}^i e^{j2m\Omega t} \tag{15b}$$

where $\mathbf{u}_{r(m)}^i, \hat{\mathbf{u}}_{r(m)}^i$, $\mathbf{v}_{r(m)}^i$, and $\hat{\mathbf{v}}_{r(m)}^i$ are the complex Fourier coefficient vectors associated with the complex harmonic function of $e^{j2m\Omega t}$.

In Eqs. (14) and (15), we can obtain the forced response of the general rotor system (5) as follows [6]:

$$\begin{aligned} \mathbf{p}(t) &= \sum_{i=B,F} \sum_{r=-N}^{N}{}' \{\mathbf{u}(t)\eta(t)\}_r^i \\ &= \sum_{i=B,F} \sum_{r=-N}^{N}{}' \sum_{m=-\infty}^{\infty} \sum_{n=-\infty}^{\infty} \left\{ \int_0^t e^{(\mu_r^i + j2m\Omega)(t-\tau)} [\mathbf{u}_{r(m)}^i \bar{\mathbf{v}}_{r(m-n)}^{iT} \mathbf{g}_{;n}(\tau) + \mathbf{u}_{r(m)}^i \bar{\hat{\mathbf{v}}}_{r(m-n)}^{iT} \bar{\mathbf{g}}_{;-n}(\tau)] \mathrm{d}\tau \right\} \\ &= \sum_{i=B,F} \sum_{r=-N}^{N}{}' \sum_{m=-\infty}^{\infty} \sum_{n=-\infty}^{\infty} \left\{ \int_0^t e^{\lambda_{r(m)}^i (t-\tau)} [\mathbf{u}_{r(m);0}^i \bar{\mathbf{v}}_{r(m);n}^{iT} \mathbf{g}_{;n}(\tau) + \mathbf{u}_{r(m);0}^i \bar{\hat{\mathbf{v}}}_{r(m);n}^{iT} \bar{\mathbf{g}}_{;-n}(\tau)] \mathrm{d}\tau \right\} \end{aligned} \tag{16}$$

Table 1 Modal strength in terms of vector norm order

$r(m)$, $r>0$ for $\lambda^{B,F}_{r(m)}$	$\lVert\hat{\mathbf{u}}^i_{r(m);1}\rVert$ $\lVert\hat{\mathbf{v}}^i_{r(m);1}\rVert$	$\lVert\mathbf{u}^i_{r(m);-1}\rVert$ $\lVert\mathbf{v}^i_{r(m);-1}\rVert$	$\lVert\hat{\mathbf{u}}^i_{r(m);0}\rVert$ $\lVert\hat{\mathbf{v}}^i_{r(m);0}\rVert$	$\lVert\mathbf{u}^i_{r(m);0}\rVert$ $\lVert\mathbf{v}^i_{r(m);0}\rVert$	$\lVert\hat{\mathbf{u}}^i_{r(m);-1}\rVert$ $\lVert\hat{\mathbf{v}}^i_{r(m);-1}\rVert$	$\lVert\mathbf{u}^i_{r(m);1}\rVert$ $\lVert\mathbf{v}^i_{r(m);1}\rVert$
$r(0)$	$O(\delta^2\Delta)$	$O(\delta\Delta)$	$\boldsymbol{O(\Delta)}$	$\underline{\boldsymbol{O(1)}}$	$O(\delta)$	$O(\delta\Delta)$
$-r(0)$	$O(\delta\Delta)$	$O(\delta)$	$\boldsymbol{O(1)}$	$\underline{\boldsymbol{O(\Delta)}}$	$O(\delta\Delta)$	$O(\delta\Delta^2)$
$r(-1)$	$O(\Delta)$	$O(1)$	$O(\delta)$	$\underline{O(\delta\Delta)}$	$O(\delta^2\Delta)$	$O(\delta^2\Delta^2)$
$-r(1)$	$O(\delta^2\Delta^2)$	$O(\delta^2\Delta)$	$O(\delta\Delta)$	$\underline{O(\delta)}$	$O(1)$	$O(\Delta)$
$r(1)$	$O(\delta^2\Delta^3)$	$O(\delta^2\Delta^2)$	$O(\delta\Delta^2)$	$\underline{O(\delta\Delta)}$	$O(\Delta)$	$O(1)$
$-r(-1)$	$O(1)$	$O(\Delta)$	$O(\delta\Delta)$	$\underline{\underline{O(\delta\Delta^2)}}$	$O(\delta^2\Delta^2)$	$O(\delta^2\Delta^3)$

The underlined indicate the representative modal strengths; $O(1)$ is for *strong* modes and others for *weak* modes. The bold identify the modes belonging to cluster 0, which are used to resolve the indefiniteness of Poincare exponents.

where the modulated force vector with the complex harmonic function of frequency $2n\Omega$ is defined as

$$\mathbf{g}_{;n}(t) \equiv \mathbf{g}(t)e^{j2n\Omega t}$$

Here, the alternative Poincare exponents $\lambda^i_{r(m)} \equiv \mu^i_r + j2m\Omega = \sigma_{r(m)} + j\omega_{r(m)}$, $\sigma_{r(m)}$, and $\omega_{r(m)}$ being the real and imaginary parts, respectively, are referred to as the modal frequencies, and $\mathbf{u}^i_{r(m);n} \equiv \mathbf{u}^i_{r(m-n)}$ and $\mathbf{v}^i_{r(m);n} \equiv \mathbf{v}^i_{r(m-n)}$ are the corresponding constant modal vectors with the relations [6],

$$\bar{\mathbf{u}}^i_{-r(-m);n} = \hat{\mathbf{u}}^i_{r(m);n}, \quad \bar{\mathbf{v}}^i_{-r(-m);n} = \hat{\mathbf{v}}^i_{r(m);n}, \quad \lambda^i_{r(m)} = \bar{\lambda}^i_{-r(-m)} \tag{17}$$

The subscript $r(m)$ refers to the rth eigen solution in cluster m, which consists of only the set of eigensolutions associated with the modulation index m, or equivalently, with the shifted eigenvalues by $j2m\Omega$.

Fourier transform of Eq. (16) leads to

$$\begin{aligned}\mathbf{P}(j\omega) &= \sum_{n=-\infty}^{\infty}\left\{\left[\sum_{i=B,F}\sum_{r=-N}^{N}{}'\sum_{m=-\infty}^{\infty}\frac{\mathbf{u}^i_{r(m);0}\bar{\mathbf{v}}^{iT}_{r(m);n}}{j\omega-\lambda^i_{r(m)}}\right]\mathbf{G}_{;n}(j\omega)\right.\\ &\left.+\left[\sum_{i=B,F}\sum_{r=-N}^{N}{}'\sum_{m=-\infty}^{\infty}\frac{\mathbf{u}^i_{r(m);0}\bar{\hat{\mathbf{v}}}^{iT}_{r(m);n}}{j\omega-\lambda^i_{r(m)}}\right]\hat{\mathbf{G}}_{;-n}(j\omega)\right\}\\ &= \sum_{n=-\infty}^{\infty}\{\mathbf{H}_{\mathbf{g}_{;n}\mathbf{p}}(j\omega)\mathbf{G}_{;n}(j\omega)+\mathbf{H}_{\bar{\mathbf{g}}_{;-n}\mathbf{p}}(j\omega)\hat{\mathbf{G}}_{;-n}(j\omega)\}\end{aligned} \tag{18}$$

where the Fourier transforms of the modulated excitation vectors are given by

$$\mathbf{G}_{;n}(j\omega) = \mathbf{G}\{j(\omega-2n\Omega)\}, \quad \hat{\mathbf{G}}_{;n}(j\omega) = \hat{\mathbf{G}}\{j(\omega+2n\Omega)\}$$

Here, $\mathbf{P}(j\omega)$, $\mathbf{G}(j\omega)$, and $\hat{\mathbf{G}}(j\omega)$ are the Fourier transforms of $\mathbf{p}(t)$, $\mathbf{g}(t)$, and $\bar{\mathbf{g}}(t)$, respectively. Among an infinite number of dFRMs defined in Eq. (18), we introduce four dFRMs that are important in characterizing the system asymmetry and anisotropy, as follows [6,17]:

$$\mathbf{H}_{\mathbf{gp}}(j\omega) = \mathbf{H}_{\mathbf{g}_{;0}\mathbf{p}}(j\omega) = \sum_{m=-\infty}^{\infty}\sum_{i=B,F}\sum_{r=-N}^{N}{}'\left[\frac{\mathbf{u}^i_{r(m);0}\bar{\mathbf{v}}^{iT}_{r(m);0}}{j\omega-\lambda^i_{r(m)}}\right]$$

$$\mathbf{H}_{\hat{\mathbf{g}}\mathbf{p}}(j\omega) = \mathbf{H}_{\bar{\mathbf{g}}_{;0}\mathbf{p}}(j\omega) = \sum_{m=-\infty}^{\infty}\sum_{i=B,F}\sum_{r=-N}^{N}{}'\left[\frac{\mathbf{u}^i_{r(m);0}\mathbf{v}^{iT}_{-r(-m);0}}{j\omega-\lambda^i_{r(m)}}\right]$$

$$\mathbf{H}_{\check{\mathbf{g}}\mathbf{p}}(j\omega) = \mathbf{H}_{\bar{\mathbf{g}}_{;-1}\mathbf{p}}(j\omega) = \sum_{m=-\infty}^{\infty}\sum_{i=B,F}\sum_{r=-N}^{N}{}'\left[\frac{\mathbf{u}^i_{r(m);0}\bar{\mathbf{v}}^{iT}_{r(m);-1}}{j\omega-\lambda^i_{r(m)}}\right] \tag{19}$$

Here, $\mathbf{H}_{\mathbf{gp}}(j\omega)$ is referred to as the normal dFRM that represents the system symmetry, $\mathbf{H}_{\hat{\mathbf{g}}\mathbf{p}}(j\omega)$ is referred to as the reverse dFRM that represents the effect of system anisotropy, and $\mathbf{H}_{\bar{\mathbf{g}}\mathbf{p}}(j\omega)$ and $\mathbf{H}_{\check{\mathbf{g}}\mathbf{p}}(j\omega)$ are referred to as the modulated dFRMs that represent the effect of system asymmetry and the coupled effect of both system anisotropy and asymmetry, respectively.

In this direct modal analysis approach for the periodically time-varying parameter system (1), the eigenvalues and the corresponding periodically time-varying eigenvectors can be analytically obtained with the rotational speed (Ω) varied. However, the closed form solutions are limited only to a few simple cases because of mathematical complexity. For most of practical applications, numerical approach is taken first to obtain the T periodic modal (adjoint) vectors, from which the constant Fourier coefficient vectors, i.e., the constant modal (adjoint) vectors, are derived [6]. Although the above procedure looks like a novel, analytical approach, one of its critical drawbacks is the numerical instability for large order systems, since it may suffer from accumulated error with extensive numerical integration processes [24]. It also requires an extra procedure to fix the problem of indefiniteness with the Poincare exponents and the corresponding T periodic modal vectors, which is explained in Appendix A. An alternative way of improving the numerical accuracy and bypassing the indefiniteness is to develop a direct calculation method of the constant modal (adjoint) vectors by constructing the Hill's infinite order matrix [6], which is taken in this work.

2.2 Modal Strength [17]. For general rotors with weak asymmetry δ and anisotropy Δ, the terms $\mathbf{M_b}$, $\mathbf{C_b}$, $\mathbf{K_b}$, $\mathbf{M_r}$, $\mathbf{C_r}$, and $\mathbf{K_r}$ in Eq. (1) can be replaced by $\Delta\mathbf{M_b}$, $\Delta\mathbf{C_b}$, $\Delta\mathbf{K_b}$, $\delta\mathbf{M_r}$, $\delta\mathbf{C_r}$, and $\delta\mathbf{K_r}$. Then, we can define the strength of a mode in terms of its vector norm order, as shown in Table 1 [17]. The modes with reference norm order of 1, $O(1)$, (smaller than 1) may be referred to as the "strong (weak) modes," because the contribution of a modal response to the total response will be proportional to the corresponding modal vector norm. The modes with reference norm order of 1, Δ, and δ are associated with symmetry, anisotropy, and asymmetry of the system, respectively, and the rest of modes are associated with the coupling of asymmetry and anisotropy. The weak modes tend to vanish as the degree of anisotropy and asymmetry diminishes. In particular, the modes of the coupled anisotropy and asymmetry are vulnerable to the degree of both asymmetry and anisotropy, so that they are not likely to be easily captured in practice.

3 An Enhanced Whirl Speed Chart: Lee Diagram

3.1 Enhanced Campbell Diagram. For complete understanding of dynamics of a rotating machine, it is required to have the full knowledge on the eigenvalues and eigenvectors, and the disturbing forces of the rotor. On the other hands, forces such as mass imbalance distribution and external torques may not be known in detail except the dominant frequency components, unless the machine goes through extensive force identification processes. The Campbell diagram (whirl speed chart), which has long been an important tool in the design and operation of rotating machinery, mostly plots the imaginary part of eigenvalues and the incomplete but useful frequency information of probable external disturbances, which is known as order lines. Thus, from the Campbell diagrams drawn for rotating machines, engineers can understand which modes are likely to be excited by the excitation sources of interest, which speed regions are safe for operation, and so on. However, it may lead to erroneous interpretation on the role of modes in the response prediction, unless their relative stability (real part of eigenvalues) and strength (norm of eigenvectors) are clearly addressed.

The Campbell diagram had been invented by W. E. Campbell in 1924 [8] and widely adopted in the design and operation of rotating machines. According to Campbell, the diagram plots the natural frequencies against the rotational speed, along with the force order lines. The intersections of the force order lines and the natural frequencies indicate, not the actual, but the potential resonances, which ought to be avoided in actual operation of the machines. The obvious drawback of the Campbell diagram is that it is very conservative in prediction of possible resonances, because it only takes the information of the rotational speed-dependent natural frequencies, which are the imaginary part of eigenvalues, and the order of all possible excitation sources. It lacks the information on stability, which is related to the real part of eigenvalues, and modal and adjoint vectors which can be available even before the manufacture or installation of the machines. In other words, the Campbell diagram does not differentiate the importance or potential severity of modes, equally treating all modes.

The strength of a mode can be indicated, as given in Table 1, by the vector norm of the corresponding modal vector independent of the nature of the excitation force. Thus, the Campbell diagram incorporated with modal strength can be used to better identify the potential danger of the machine in design and operation. The intersections of the force order lines with strong modes should be treated more important than those with weak modes as the potential severity of a mode depends on the magnitude of the corresponding modal strength. However, the enhanced Campbell diagram still lacks the information on stability or damping of the system. Another difficulty is in the computation of bi-orthonormalized modal and adjoint vectors. Following the computational procedure in Sec. 2.1, we can solve, without a difficulty, for the eigensolutions consisting of eigenvalues, modal, and adjoint vectors, with Ω varied. However, modal and adjoint vectors should be bi-orthonormalized with the constraint that they are of the same vector norm [6].

3.2 Matrix Norm as a Severity Measure. Frequency response is the input to output relation in the frequency domain, or it can be interpreted as the dynamic gain between the input and the output, for any order lines of unknown forces. It is the potential severity of the modal responses to unknown harmonic excitation, which includes the information on modal frequencies and dampings, modal, and adjoint vectors, and the forcing line order. The dFRMs defined in Eq. (19) carry too much information so that direct use of the dFRMs is not practical. Thus, we can introduce the infinity-matrix norm of the dFRMs as a simple, yet practical measure of potential severity of modes, i.e.,

$$
\begin{aligned}
L_{11}(\omega,\Omega) &\equiv \|\mathbf{H}_{\mathbf{gp}}(j\omega)\|_\infty = \|\mathbf{H}_{\mathbf{g}_{;0}\mathbf{p}}(j\omega)\|_\infty \\
&= \left\| \sum_{m=-\infty}^{\infty} \sum_{i=B,F} \sum_{r=-N}^{N}{}' \left[\frac{\mathbf{u}^i_{r(m);0}\overline{\mathbf{v}}^{iT}_{r(m);0}}{j\omega-\lambda^i_{r(m)}} \right] \right\|_\infty \\
L_{12}(\omega,\Omega) &\equiv \|\mathbf{H}_{\mathbf{\dot{g}p}}(j\omega)\|_\infty = \|\mathbf{H}_{\mathbf{\dot{g}}_{;0}\mathbf{p}}(j\omega)\|_\infty \\
&= \left\| \sum_{m=-\infty}^{\infty} \sum_{i=B,F} \sum_{r=-N}^{N}{}' \left[\frac{\mathbf{u}^i_{r(m);0}\mathbf{v}^{iT}_{-r(-m);0}}{j\omega-\lambda^i_{r(m)}} \right] \right\|_\infty \\
L_{21}(\omega,\Omega) &\equiv \|\mathbf{H}_{\mathbf{\ddot{g}p}}(j\omega)\|_\infty = \|\mathbf{H}_{\mathbf{\ddot{g}}_{;-1}\mathbf{p}}(j\omega)\|_\infty \\
&= \left\| \sum_{m=-\infty}^{\infty} \sum_{i=B,F} \sum_{r=-N}^{N}{}' \left[\frac{\mathbf{u}^i_{r(m);0}\mathbf{v}^{iT}_{-r(-m);-1}}{j\omega-\lambda^i_{r(m)}} \right] \right\|_\infty \\
L_{22}(\omega,\Omega) &\equiv \|\mathbf{H}_{\mathbf{\ddot{g}p}}(j\omega)\|_\infty = \|\mathbf{H}_{\mathbf{g}_{;-1}\mathbf{p}}(j\omega)\|_\infty \\
&= \left\| \sum_{m=-\infty}^{\infty} \sum_{i=B,F} \sum_{r=-N}^{N}{}' \left[\frac{\mathbf{u}^i_{r(m);0}\overline{\mathbf{v}}^{iT}_{r(m);-1}}{j\omega-\lambda^i_{r(m)}} \right] \right\|_\infty
\end{aligned} \tag{20}
$$

The matrix norm defined above is theoretically perfect, but it is computationally inefficient. Although the modal and adjoint vectors are not required to be bi-orthonormalized, the matrix norm has to be taken after summing up all modal responses. Note here that the infinity norm of dFRMs is similar in concept to the H_∞ control, in the sense that the design and control of an interested system is based on its maximum possible dynamic gain in the frequency domain. This idea can be an excellent design tool for rotating machinery, using the concept of the worst-case response prediction.

Using the results in Table 1, we introduce the upper bound of the norm of the dFRMs, omitting the symbol ∞ for notational convenience, as

$$
\begin{aligned}
L_{11}(\omega,\Omega) \le \hat{L}_{11}(\omega,\Omega) &\equiv \sum_{r=1}^{N} \sum_{i=B,F} \left\{ \frac{\|\mathbf{u}^i_{r(0);0}\overline{\mathbf{v}}^{iT}_{r(0);0}\|}{|j\omega-\lambda^i_{r(0)}|} \right. \\
&+ \frac{\|\mathbf{u}^i_{r(-1);0}\overline{\mathbf{v}}^{iT}_{r(-1);0}\|}{|j\omega-\lambda^i_{r(-1)}|} + \frac{\|\mathbf{u}^i_{r(1);0}\overline{\mathbf{v}}^{iT}_{r(1);0}\|}{|j\omega-\lambda^i_{r(1)}|} + \frac{\|\mathbf{u}^i_{-r(0);0}\overline{\mathbf{v}}^{iT}_{-r(0);0}\|}{|j\omega-\lambda^i_{-r(0)}|} \\
&\left. + \frac{\|\mathbf{u}^i_{-r(-1);0}\overline{\mathbf{v}}^{iT}_{-r(-1);0}\|}{|j\omega-\lambda^i_{-r(-1)}|} + \frac{\|\mathbf{u}^i_{-r(1);0}\overline{\mathbf{v}}^{iT}_{-r(1);0}\|}{|j\omega-\lambda^i_{-r(1)}|} \right\} \\
&\sim \sum_{r=1}^{N} \sum_{i=B,F} \left\{ \frac{\boldsymbol{O}(\mathbf{1})}{|j\omega-\lambda^i_{r(0)}|} + \frac{O(\delta^2\Delta^2)}{|j\omega-\lambda^i_{r(-1)}|} + \frac{O(\delta^2\Delta^2)}{|j\omega-\lambda^i_{r(1)}|} \right. \\
&\left. + \frac{O(\Delta^2)}{|j\omega-\lambda^i_{-r(0)}|} + \frac{O(\delta^2\Delta^4)}{|j\omega-\lambda^i_{-r(-1)}|} + \frac{O(\delta^2)}{|j\omega-\lambda^i_{-r(1)}|} \right\}
\end{aligned} \tag{21a}
$$

$$
\begin{aligned}
L_{12}(\omega,\Omega) \le \hat{L}_{12}(\omega,\Omega) &\equiv \sum_{r=1}^{N} \sum_{i=B,F} \left\{ \frac{\|\mathbf{u}^i_{r(0);0}\overline{\hat{\mathbf{v}}}^{iT}_{r(0);0}\|}{|j\omega-\lambda^i_{r(0)}|} \right. \\
&+ \frac{\|\mathbf{u}^i_{r(-1);0}\overline{\hat{\mathbf{v}}}^{iT}_{r(-1);0}\|}{|j\omega-\lambda^i_{r(-1)}|} + \frac{\|\mathbf{u}^i_{r(1);0}\overline{\hat{\mathbf{v}}}^{iT}_{r(1);0}\|}{|j\omega-\lambda^i_{r(1)}|} + \frac{\|\mathbf{u}^i_{-r(0);0}\overline{\hat{\mathbf{v}}}^{iT}_{-r(0);0}\|}{|j\omega-\lambda^i_{-r(0)}|} \\
&\left. + \frac{\|\mathbf{u}^i_{-r(1);0}\overline{\hat{\mathbf{v}}}^{iT}_{-r(-1);0}\|}{|j\omega-\lambda^i_{-r(-1)}|} + \frac{\|\mathbf{u}^i_{-r(1);0}\overline{\hat{\mathbf{v}}}^{iT}_{-r(-1);0}\|}{|j\omega-\lambda^i_{-r(1)}|} \right\} \\
&\sim \sum_{r=1}^{N} \sum_{i=B,F} \left\{ \frac{\boldsymbol{O}(\boldsymbol{\Delta})}{|j\omega-\lambda^i_{r(0)}|} + \frac{O(\delta^2\Delta)}{|j\omega-\lambda^i_{r(-1)}|} + \frac{O(\delta^2\Delta^3)}{|j\omega-\lambda^i_{r(1)}|} \right. \\
&\left. + \frac{\boldsymbol{O}(\boldsymbol{\Delta})}{|j\omega-\lambda^i_{-r(0)}|} + \frac{O(\delta^2\Delta^3)}{|j\omega-\lambda^i_{-r(-1)}|} + \frac{O(\delta^2\Delta)}{|j\omega-\lambda^i_{-r(1)}|} \right\}
\end{aligned} \tag{21b}
$$

$$L_{21}(\omega,\Omega) \le \hat{L}_{21}(\omega,\Omega) \equiv \sum_{r=1}^{N} \sum_{i=B,F} \left\{ \frac{\|\mathbf{u}^i_{r(0);0} \bar{\hat{\mathbf{v}}}^{iT}_{r(0);-1}\|}{|j\omega - \lambda^i_{r(0)}|} + \frac{\|\mathbf{u}^i_{r(-1);0} \bar{\hat{\mathbf{v}}}^{iT}_{r(-1);-1}\|}{|j\omega - \lambda^i_{r(-1)}|} + \frac{\|\mathbf{u}^i_{r(1);0} \bar{\hat{\mathbf{v}}}^{iT}_{r(1);-1}\|}{|j\omega - \lambda^i_{r(1)}|} + \frac{\|\mathbf{u}^i_{-r(0);0} \bar{\hat{\mathbf{v}}}^{iT}_{-r(0);-1}\|}{|j\omega - \lambda^i_{-r(0)}|} + \frac{\|\mathbf{u}^i_{-r(-1);0} \bar{\hat{\mathbf{v}}}^{iT}_{-r(-1);-1}\|}{|j\omega - \lambda^i_{-r(-1)}|} + \frac{\|\mathbf{u}^i_{-r(1);0} \bar{\hat{\mathbf{v}}}^{iT}_{-r(1);-1}\|}{|j\omega - \lambda^i_{-r(1)}|} \right\} \sim \sum_{r=1}^{N} \sum_{i=B,F} \left\{ \frac{\boldsymbol{O(\delta)}}{|j\omega - \lambda^i_{r(0)}|} + \frac{O(\delta^3\Delta^2)}{|j\omega - \lambda^i_{r(-1)}|} + \frac{O(\delta\Delta^2)}{|j\omega - \lambda^i_{r(1)}|} + \frac{O(\delta\Delta^2)}{|j\omega - \lambda^i_{-r(0)}|} + \frac{O(\delta^3\Delta^4)}{|j\omega - \lambda^i_{-r(-1)}|} + \frac{\boldsymbol{O(\delta)}}{|j\omega - \lambda^i_{-r(1)}|} \right\} \tag{21c}$$

$$L_{22}(\omega,\Omega) \le \hat{L}_{22}(\omega,\Omega) \equiv \sum_{r=1}^{N} \sum_{i=B,F} \left\{ \frac{\|\mathbf{u}^i_{r(0);0} \bar{\mathbf{v}}^{iT}_{r(0);-1}\|}{|j\omega - \lambda^i_{r(0)}|} + \frac{\|\mathbf{u}^i_{r(-1);0} \bar{\mathbf{v}}^{iT}_{r(-1);-1}\|}{|j\omega - \lambda^i_{r(-1)}|} + \frac{\|\mathbf{u}^i_{r(1);0} \bar{\mathbf{v}}^{iT}_{r(1);-1}\|}{|j\omega - \lambda^i_{r(1)}|} + \frac{\|\mathbf{u}^i_{-r(0);0} \bar{\mathbf{v}}^{iT}_{-r(0);-1}\|}{|j\omega - \lambda^i_{-r(0)}|} + \frac{\|\mathbf{u}^i_{-r(-1);0} \bar{\mathbf{v}}^{iT}_{-r(-1);-1}\|}{|j\omega - \lambda^i_{-r(-1)}|} + \frac{\|\mathbf{u}^i_{-r(1);0} \bar{\mathbf{v}}^{iT}_{-r(1);-1}\|}{|j\omega - \lambda^i_{-r(1)}|} \right\} \sim \sum_{r=1}^{N} \sum_{i=B,F} \left\{ \frac{\boldsymbol{O(\delta\Delta)}}{|j\omega - \lambda^i_{r(0)}|} + \frac{O(\delta^3\Delta^3)}{|j\omega - \lambda^i_{r(-1)}|} + \frac{\boldsymbol{O(\delta\Delta)}}{|j\omega - \lambda^i_{r(1)}|} + \frac{O(\delta\Delta^3)}{|j\omega - \lambda^i_{-r(0)}|} + \frac{O(\delta^3\Delta^5)}{|j\omega - \lambda^i_{-r(-1)}|} + \frac{\boldsymbol{O(\delta\Delta)}}{|j\omega - \lambda^i_{-r(1)}|} \right\} \tag{21d}$$

where the modes with the bold-faced norm order indicate the dominant modes in the associated dFRMs. The computation of $\hat{L}_{ik}(\omega,\Omega), i,k=1,2$, is much more convenient than direct computation of the infinity-matrix norms $L_{ik}(\omega,\Omega), i,k=1,2$, because the former are computed for residue matrices associated with every modes and then summed up to form the upper bounds to the latter. The upper bounds are still meaningful because they not only closely approximate the infinity-matrix norm of dFRMs, but they can be understood as a design concept based on a worst-case response prediction. The computational effort required for $L_{ik}(\omega,\Omega)$ and $\hat{L}_{ik}(\omega,\Omega)$, $i,k=1,2$ is discussed in Appendix B.

In Eq. (21), we can define a 2×2 matrix function of two variables, ω and Ω, as

$$\mathbf{L}(\omega,\Omega) = \begin{bmatrix} L_{11}(\omega,\Omega) & L_{12}(\omega,\Omega) \\ L_{21}(\omega,\Omega) & L_{22}(\omega,\Omega) \end{bmatrix} \tag{22}$$

From the previous discussions, we make the following conclusions.

1. $L_{11}(\omega,\Omega)$ is useful to identify the importance of modes in potential contribution to unknown forced response.
2. $L_{12}(\omega,\Omega)$ is a good indicator of the degree of anisotropy and presence of the modes due to system anisotropy.
3. $L_{21}(\omega,\Omega)$ is a good indicator of the degree of asymmetry and presence of the modes due to system asymmetry.
4. $L_{22}(\omega,\Omega)$ identifies the coupled effect of system anisotropy and asymmetry.

Here, the plot of a set of four scalar functions taken from $\mathbf{L}(\omega,\Omega)$ (or $\hat{\mathbf{L}}(\omega,\Omega)$ as an approximation) will be referred to as the Lee diagram. $L_{11}(\omega,\Omega)$, which is most important among the four scalar functions, can be directly used as an efficient measure of the possibility of resonance at the various modal frequencies of a general rotor in its design and operation stage.

3.3 Discussions. As cited in Sec. 1, the Campbell diagram plots the speed-dependent natural frequency of a rotor, superimposed by the possible excitation order lines, whose intersections represent the possible occurrence of resonances. It treats all natural frequencies equally so that, for a practical rotor with either many degrees of freedom or many sources of excitations, their intersections often turn out to be too many in number to be reflected in design and operation of the rotor. In other words, the diagram is so conservative in prediction of possible resonances that it often fails in providing practice engineers with any meaningful information. The primary reason is that, besides the excitation order lines, it takes only the imaginary part ($\omega_{r(m)}$), so-called the modal frequency, of the eigenvalues, among the eigensolutions that are obtained from modal analysis of the rotor. The missing information in the conventional Campbell diagram is the real part ($\sigma_{r(m)}$) of the eigenvalues (or equivalently, the modal damping, logarithmic decrement or stability) and the eigenvectors (modal and adjoint vectors, $\mathbf{u}^i_{r(m)}$ and $\mathbf{v}^i_{r(m)}$, or equivalently, modal responses). Root locus plots the trajectory of $\sigma_{r(m)}$ as the abscissa, and $\omega_{r(m)}$ as the ordinate with the rotational speed Ω varied [25]. However, the root locus, although the stability information is implemented, is still vague in clearly identifying the important possible resonances.

The frequency response matrix (FRM) not only includes all the available sources of information obtained from modal analysis such as the real and imaginary parts of eigenvalues, eigenvectors, but also it normally represents the multi-input and multi-output relationship, which is the dynamic gain (influence coefficient) matrix of the rotor system. Thus, FRM can be taken as an ideal measure for severity of possible resonances to the excitations of known frequency (order lines). On the other hand, FRM, as a measure (matrix function of ω and Ω), is too difficult to handle because it includes as many frequency response functions (FRFs) as the product of the number of input and output. The infinity norm of FRM instead is a single scalar function of frequency and rotational speed, which corresponds to the maximum possible dynamic gain, i.e., the predicted worst response of the rotor.

Another issue to discuss is what happens when we conduct the modal analysis of a general rotor in the conventional real coordinates, as majority of, except a few, researchers have taken. We will obtain the same original and complex conjugate eigenvalues as before, irrespective of the choice of real or complex coordinates (except for isotropic rotors in the complex coordinates where the complex conjugate eigenvalues are not allowed [3]). However, the corresponding modal and adjoint vectors are not so clearly identified as before, because in the real coordinates the modal vectors associated with the original and complex conjugate eigenvalues always form complex conjugate pairs [3]. It means that the norm order analysis of modal vectors leads to the same order of magnitude, irrespective of the nature of the original and complex conjugate modes. When formulated in the complex coordinates, the norm of the original modal vector is of order of magnitude, whereas the norm of the complex conjugate modal vector becomes of order of smallness, because the complex conjugate modes are treated as the parasitic modes to the original ones.

4 Illustrative Examples

In this section, we consider three rotors: an anisotropic rigid rotor, a simple general rotor, and a commercial generator. The anisotropic rigid rotor is taken as an example in order to demon-

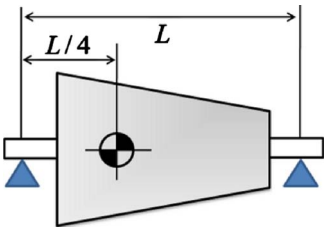

Fig. 1 An anisotropic rigid rotor

strate construction of the enhanced Campbell diagram incorporated with modal strength and the infinity norm of dFRFs. The simple general rotor is a perfect example for demonstration of the power of the Lee diagram against the conventional Campbell diagram, because the general rotor represents the real rotating machinery in general, which is characterized by both anisotropy and asymmetry occurring in practice. The third example, a commercial generator, is taken to demonstrate the practicality of Lee diagram with real rotors. In the examples, the Lee diagrams have been normalized as $L_{ik}(\omega,\Omega)/L_{11}(0,0)$, $i,k=1,2$, for convenience in scale.

4.1 Anisotropic Rigid Rotor. Consider an anisotropic rigid rotor consisting of a symmetric rigid rotor supported by identical orthotropic bearings at ends, as shown in Fig. 1, whose equation of motion is given in Appendix C [3]. Figure 2 shows the Campbell diagram with the unbalance force order line (broken line in the figure), indicating four possible occurrence of forward synchronous resonance and treating all modes, translatory and conical, equally. Figure 3(*a*) is the enhanced Campbell diagram by identifying the strong (weak) modes by thick (thin) lines. Figure 3(*b*) shows the infinity vector norm of the bi-orthonormalized complex modal vectors. From the figure, it is evident that as the rotational speed increases, the norm order associated with two original modal vectors remains as the order of magnitude, whereas that with their complex conjugate modes decreases rapidly, becoming the order of smallness, $\Delta=\Delta k/k=0.04$, i.e., the degree of anisotropy in bearing stiffness. Figures 3(*a*) and 3(*b*) imply that the number of significant modes associated with possible occurrence of forward synchronous resonance is reduced to two from four. For the comparison purpose, the infinity norm of the modal vectors defined in the real coordinates is plotted in Fig. 3(*c*). Note that the norm of all modes becomes the order of magnitude, so that there is no way to differentiate the strength of original modes from their complex conjugates in the real coordinates.

In Figs. 4(*a*) and 4(*b*), the thin lines are the four sets of normal and reverse dFRFs, respectively, at $\Omega=2$ for the anisotropic rigid rotor. The thick broken line corresponds to the infinity norm of

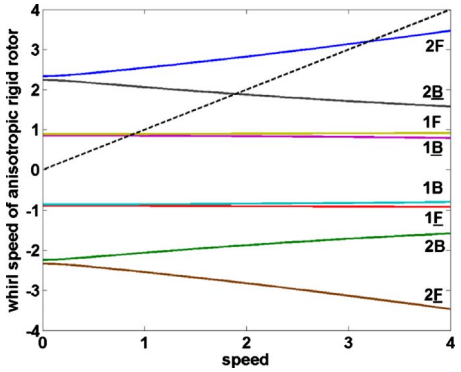

Fig. 2 Campbell diagram for the anisotropic rotor: unbalance force (----); F(B): forward (backward) mode; under-bar: complex conjugate mode

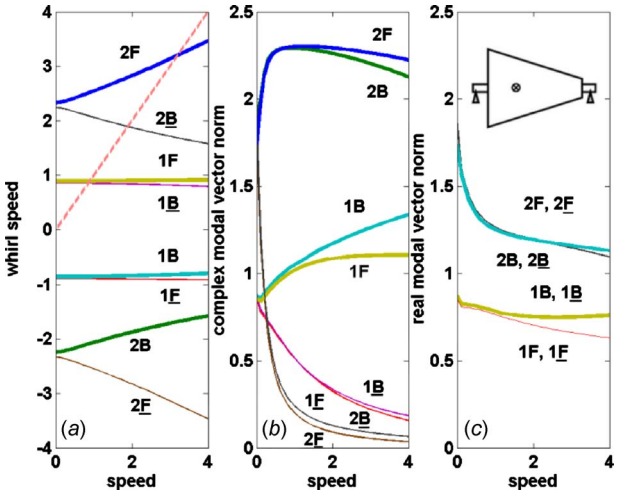

Fig. 3 (*a*) Campbell diagram incorporated with modal strength, (*b*) complex, and (*c*) real modal vector norm for the anisotropic rigid rotor

dFRMs, $L_{11}(\omega,\Omega)$ and $L_{12}(\omega,\Omega)$. And, $\hat{L}_{11}(\omega,\Omega)$ and $\hat{L}_{12}(\omega,\Omega)$ (indicated by thick solid lines in the figure) are the upper bound to the infinity norm of dFRMs, which resemble the infinity norm of dFRFs near resonances. The small discrepancies of the upper bound from the infinity norm near antiresonances are not considered important, because we are mostly interested in the dynamic behavior of the rotor near resonances. Note that the plot of $L_{11}(\omega,\Omega)$ clearly identifies the four dominant original modes and $L_{12}(\omega,\Omega)$ indicates additional four complex conjugate modes that are present due to the system anisotropy. For comparison, the infinity norm of the 4×4 FRM, along with the 16 FRFs defined in the real coordinates is plotted in Fig. 4(*c*), which fails in identifying the important modes. Figures 5(*a*) and 5(*b*) are the plots of the Lee diagram consisting of $L_{11}(\omega,\Omega)$ and $L_{12}(\omega,\Omega)$, for the anisotropic rigid rotor. Note that $L_{11}(\omega,\Omega)$ is the major plot, which indicates the strong modes clearly, whereas $L_{12}(\omega,\Omega)$ can be used

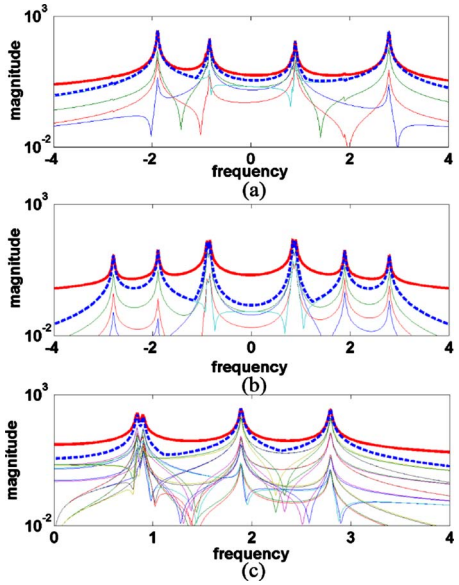

Fig. 4 (*a*) Normal and (*b*) reverse dFRFs, and (*c*) FRFs for the anisotropic rigid rotor: —dFRFs or FRFs; ·····Lee diagram; —Upper bound to Lee diagram

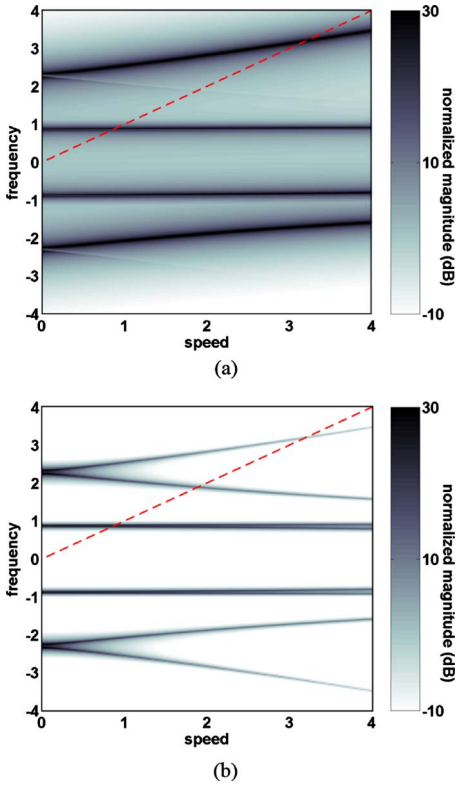

Fig. 5 Lee diagram for the anisotropic rigid rotor (*a*) $L_{11}(\omega,\Omega)$ and (*b*) $L_{12}(\omega,\Omega)$

to identify the weak modes appearing due to presence of system anisotropy. For anisotropic (asymmetric) rotors, $L_{21}(\omega,\Omega)$ and $L_{22}(\omega,\Omega)$ ($L_{12}(\omega,\Omega)$ and $L_{22}(\omega,\Omega)$) vanish.

4.2 Simple General Rotor. Now consider a simple general rotor system (see the insert in Fig. 6), whose equation of motion is written as follows [3,17]:

$$\ddot{p}(t) + (2\varsigma - j\alpha\Omega)\dot{p}(t) + p(t) + \delta e^{j2\Omega t}\bar{p}(t) + \Delta\bar{p}(t) = g(t)$$

where $p(t)=y(t)+jz(t)$ is the complex angular displacement of the rotor defined in the stationary coordinates (y,z). The above equation includes the gyroscopic moment $(\alpha\Omega)$, external damping (ς), bearing anisotropy (Δ), and shaft stiffness asymmetry (δ). This rotor model is very simple, yet it generally contains all the essential characteristics of practical rotors. Figure 6 shows the Campbell diagram for the general rotor with $\alpha=0.6$, $\delta=\Delta=0.1$, and $\varsigma=0.02$ as the rotational speed Ω is varied up to 3. In the figure, the

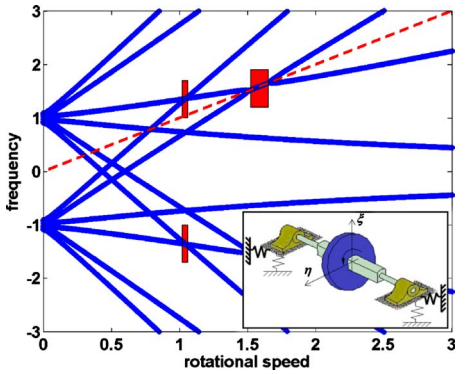

Fig. 6 Conventional Campbell diagram for the simple general rotor

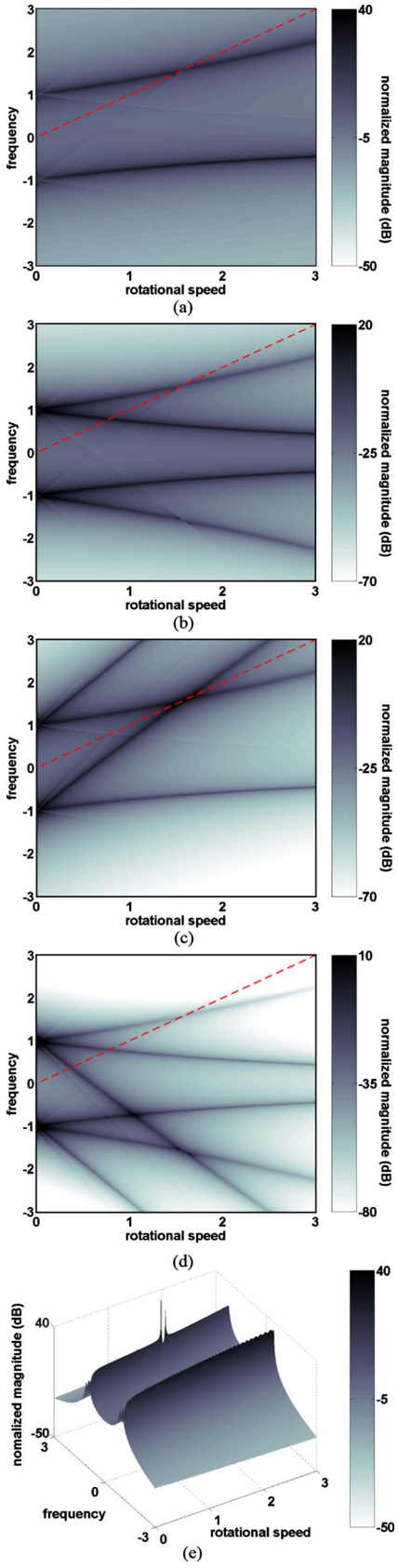

Fig. 7 Lee diagram for the simple general rotor (*a*) $L_{11}(\omega,\Omega)$, (*b*) $L_{12}(\omega,\Omega)$, (*c*) $L_{21}(\omega,\Omega)$, (*d*) $L_{22}(\omega,\Omega)$, and (*e*) three-dimensional $L_{11}(\omega,\Omega)$

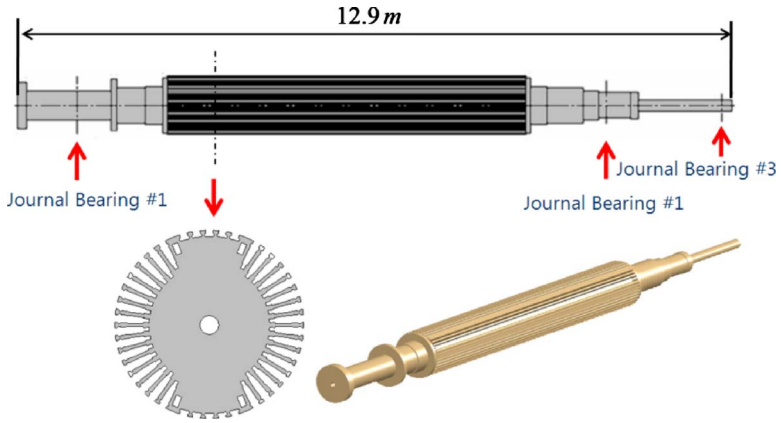

Fig. 8 Commercial two-pole generator

shaded areas indicate the instability speed regions (one near at $\Omega=1$ and another near at $\Omega=1.5$ in the figure). Note that the Campbell diagram is crowded with an infinite number (only 12 modes are shown in the figure) of modes, which may all cause resonances depending upon the type of external forces. For example, we can find six (out of twelve modes shown) possible resonant modes due to the unbalance excitation (marked by broken line) only, even for this simple general rotor model.

Figure 7 is the plot of Lee diagram, $\mathbf{L}(\omega,\Omega)$, consisting of four scalar functions, $L_{ik}(\omega,\Omega), i,k=1,2$, of ω and Ω. As before, $L_{11}(\omega,\Omega)$ successfully picks out 2 important original (strong) modes out of 12 and the severity of the corresponding modal responses is well identified by its magnitude (intensity). The gray-scale maps of $L_{11}(\omega,\Omega)$ and $L_{21}(\omega,\Omega)$ also clearly identifies the location of the two instability speed regions, incorporated with the corresponding three-dimensional plots such as $L_{11}(\omega,\Omega)$ shown in Fig. 7(*e*). The instability region near at $\Omega=1$ is hardly seen due to its narrow speed region and the presence of damping. We can conclude from $L_{11}(\omega,\Omega)$ that the rest of modes, due to the relatively small magnitude, do not play a significant role in check of possible resonances with any external forces. The plots of $L_{12}(\omega,\Omega)$ and $L_{21}(\omega,\Omega)$, together with $L_{11}(\omega,\Omega)$, detect the secondary modes appearing due to the presence of anisotropy and asymmetry in the system, respectively, which are less important than the primary strong modes. Finally, the plot of $L_{22}(\omega,\Omega)$, compared with $L_{12}(\omega,\Omega)$ and $L_{21}(\omega,\Omega)$, successfully detects the anisotropy-asymmetry coupled modes, which are considered to be far less important than the others. From the Lee diagram for the simple general rotor, we can identify two primary modes (order of magnitude) from $L_{11}(\omega,\Omega)$, two secondary modes (order of Δ) from $L_{12}(\omega,\Omega)$, two secondary modes (order of δ) from $L_{21}(\omega,\Omega)$ and many tertiary (six in the figure) modes (order of $\delta\Delta$ or higher) from $L_{22}(\omega,\Omega)$. Once the modal contributions are identified from $\mathbf{L}(\omega,\Omega)$, we can solely use $L_{11}(\omega,\Omega)$ for detection of possible resonances with external forces as we did with Campbell diagram.

4.3 Commercial Generator Model. The third example is a two-pole generator shown in Fig. 8. The commercial two-pole generator has asymmetry in the rotating part because there are many slots in the rotor for coil windings. Moreover, three journal bearings, of which bearing properties are strongly dependent upon the rotational speed, have anisotropy. The two-pole generator is modeled by finite elements of Rayleigh's beam and the coil windings are modeled by additional point masses. Figure 9 shows the conventional Campbell diagram drawn from 1000 rpm to 3960 rpm. As there are numerous modes in the Campbell diagram, it may mislead us to a wrong judgment that it is almost impossible to operate the generator near at 3600 rpm without a chance in resonance. Instead, the significance of resonances can be evaluated by modal strength as shown in Fig. 10. Primary strong modes are distinguished from numerous weak modes by their modal strength (intensity level in the figure). However, the Campbell diagram only with modal strength is very conservative in the sense that it exaggerates the role of primary strong modes, because it still lacks the information of the damping and the input to output relation of the generator.

Figure 11 plots $\hat{\mathbf{L}}(\omega,\Omega)$ instead of $\mathbf{L}(\omega,\Omega)$, for the two-pole generator due to the computational efficiency discussed in Appendix B. Note that the Lee diagrams shown in Figs. 7 and 11 are alike in nature, because the generator is indeed a typical practical

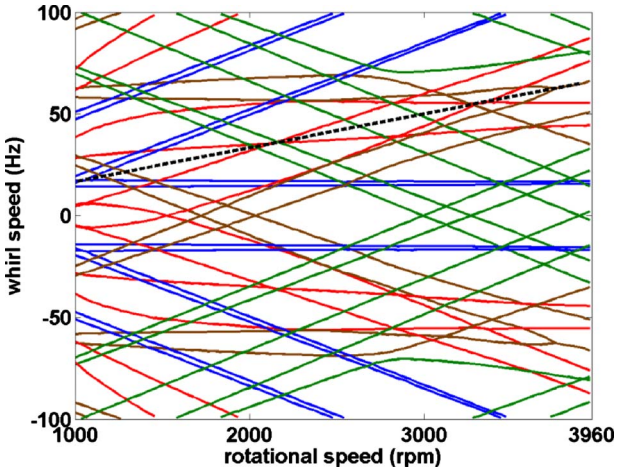

Fig. 9 Conventional Campbell diagram for two-pole generator

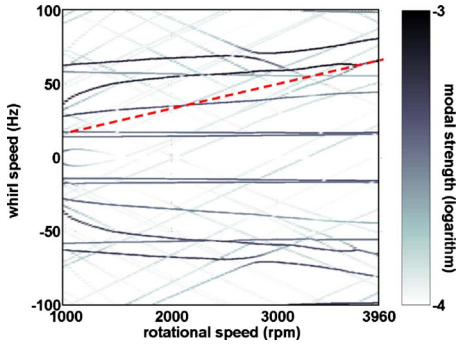

Fig. 10 Campbell diagram incorporated with modal strength for two-pole generator

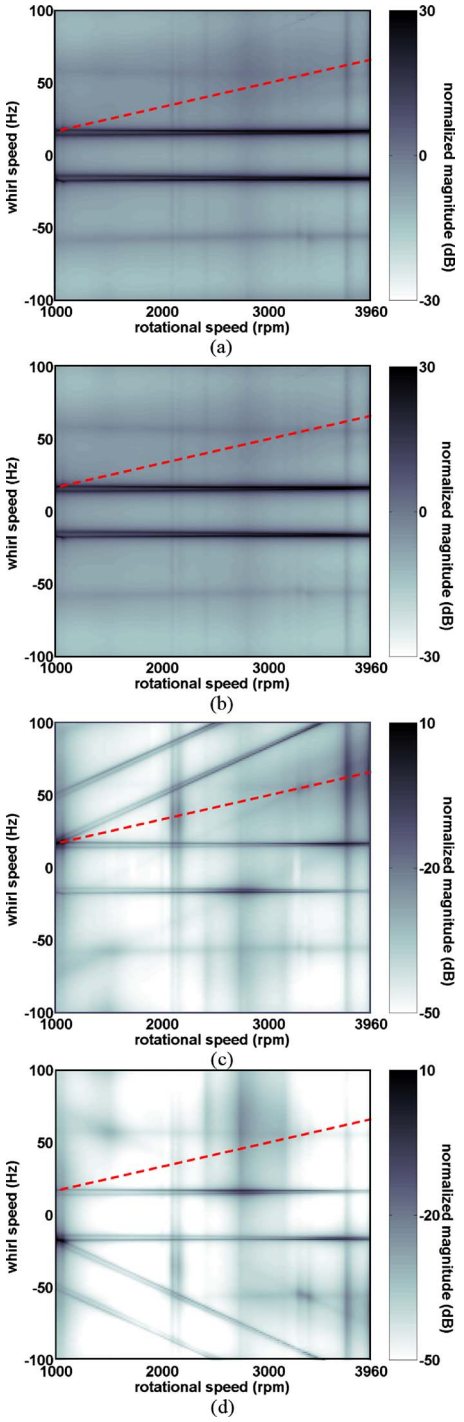

Fig. 11 Lee diagram (upper bound) for two-pole generator (*a*) $\hat{L}_{11}(\omega,\Omega)$, (*b*) $\hat{L}_{12}(\omega,\Omega)$, (*c*) $\hat{L}_{21}(\omega,\Omega)$, and (*d*) $\hat{L}_{22}(\omega,\Omega)$

example of a general rotor. Figure 11(*a*) shows $\hat{L}_{11}(\omega,\Omega)$, which represents symmetric property. The plot is the most important to evaluate the possible contribution of modes to forced responses because the symmetric property is generally much larger than the anisotropic and asymmetric property. From the plot of $\hat{L}_{11}(\omega,\Omega)$, it can be concluded that only the first translatory modes near at ± 20 Hz play an important role in the predicted forced response, although the generator system has many other strong modes, as seen in Fig. 10. Because the other strong modes except the first translatory modes are heavily damped by the three journal bearings of large damping, the potential contributions of those modes to forced responses remain insignificant, compared with the first translatory modes. Note that other strong modes near at ± 60 Hz may also have a little, if not significant, contribution to the forced responses. The magnitude of $\hat{L}_{12}(\omega,\Omega)$ is similar to that of $\hat{L}_{11}(\omega,\Omega)$. It means that the system possesses a relatively large amount of anisotropy in the journal bearing properties. The weak modes in $\hat{L}_{21}(\omega,\Omega)$ that do not appear in $\hat{L}_{11}(\omega,\Omega)$ and $\hat{L}_{12}(\omega,\Omega)$ become visible, but they have small magnitudes compared with $\hat{L}_{12}(\omega,\Omega)$ (see the use of two different scales). It is because the asymmetry of the two-pole generator is relatively small, compared with the journal bearing anisotropy. From the plots of $\hat{L}_{11}(\omega,\Omega)$ and $\hat{L}_{21}(\omega,\Omega)$, we can identify the possibility of excessive unbalance and transient response in the narrow speed region centered at about 1050 rpm, due to the presence of asymmetry in the generator rotor. The anisotropy-asymmetry coupled modes of $O(\Delta\delta)$ or smaller are well identified from $\hat{L}_{22}(\omega,\Omega)$ in Fig. 11(*d*).

5 Conclusions

Table 2 compares various diagrams in usage of available information. The order analysis for a general rotor with weak anisotropy and asymmetry and the use of the Lee diagram are successful in check for coincidence of probable excitation sources with modal frequencies of rotor, when the degree of anisotropy and asymmetry of the rotor system remains small. The smallness is not a strong assumption, because most practical rotors are either made close to axisymmetric shape or run at a relatively high operating speed, as proven in Appendix D.

The following can be concluded from use of the infinity norm of dFRMs as a measure of severity of possible resonances.

1. Lee diagram, consisting of the four plots, $L_{11}(\omega,\Omega)$, $L_{12}(\omega,\Omega)$, $L_{21}(\omega,\Omega)$, and $L_{22}(\omega,\Omega)$ clearly identifies the important modes as well as resonances of a general rotor system with either the weak rotating and stationary asymmetry or the strong skew-symmetric coupled system matrices.
2. $L_{11}(\omega,\Omega)$ readily differentiates the original (strong) modes from the complex conjugate (weak) modes.
3. $L_{12}(\omega,\Omega)$, $L_{21}(\omega,\Omega)$, and $L_{22}(\omega,\Omega)$ are useful in identifying the weak modes of less importance associated with the stationary asymmetry, the rotating asymmetry, and the coupled asymmetry of the rotor, respectively.
4. The Lee diagram can be used as a powerful design tool for rotating machinery, particularly for FEM based rotor models in their design phase.

Table 2 Comparison of diagrams in usage of available information

	Re(λ)	Im(λ)	Modal vector	Excitation
Campbell diagram	X	O	X	Order lines
Root locus	O	O	X	X
SAFE	X	O	No. of nodal diameters	Order lines
Campbell diagram with modal strength	X	O	Modal vector norm	Order lines
Lee diagram	O	O	Residue matrix norm	Order lines+maximum frequency response

5. Among others, $L_{11}(\omega,\Omega)$ alone is far superior in prediction of occurrence of possible resonances of the rotor to the conventional Campbell diagram, because it identifies the modes of paramount importance in design and operation of rotating machines.

Appendix A: Determination of Basis Poincare Exponents

According to the Floquet theory applied to a periodically time-varying linear system of period T, the Poincare exponent, μ, and the corresponding T periodic eigenvector (modal vector), $\mathbf{r}(t)$ $(\mathbf{u}_c(t))$, are indefinite, in the sense that it holds, for an arbitrary integer k,

$$e^{\mu t}\mathbf{r}(t) = e^{\mu' t}\mathbf{r}'(t) \Rightarrow e^{\mu t}\mathbf{u}_c(t) = e^{\mu' t}\mathbf{u}_c'(t) \tag{A1}$$

$$\mu' = \mu + j\frac{2\pi k}{T}, \quad \mathbf{u}_c'(t) = e^{-j\frac{2\pi k t}{T}}\mathbf{u}_c(t) \tag{A2}$$

i.e., there exist an infinite number of solutions for μ and $\mathbf{u}_c(t)$. The general rotor system (1) with weak asymmetry can be considered to be a perturbed system from the associated time invariant linear system, excluding the perturbations preceded by $e^{j2\Omega t}$ (or equivalently $e^{j2\pi t/T}$) in Eq. (1). Let us assume that the eigenvalues and the corresponding constant modal vectors of the associated constant system are μ_0 and $\mathbf{u}_{c0}$, respectively. The T periodic eigenvector, $\mathbf{u}_c(t)$ associated with Eq. (1) can be expanded in Fourier series as follows:

$$\mathbf{u}_c(t) = \mathbf{u}_{c0} + \sum_{m=-\infty}^{\infty} \delta\mathbf{u}_{c(m)} e^{j2\pi m t/T} \tag{A3}$$

Here, $\delta\mathbf{u}_{c(m)}, m=0,\pm 1,\pm 2,\pm 3,\ldots$ are the perturbation vectors to $\mathbf{u}_{c0}$. Provided that the order of $\|\delta\mathbf{u}_{c(m)}\|/\|\mathbf{u}_{c0}\|$, $m=0,\pm 1,\pm 2,\pm 3,\ldots$ are δ or smaller, referring to Sec. 2.2 and Table 1, the basis of Poincare exponents and the corresponding T periodic modal vectors can be formed as follows.

(1) Obtain an arbitrary Poincare exponent, μ', and the corresponding T periodic vector, $\mathbf{u}_c'(t)$.
(2) Expand $\mathbf{u}_c'(t)$ in Fourier series as

$$\mathbf{u}_c'(t) = e^{j2\pi k t/T}\left[\mathbf{u}_{c0} + \sum_{m=-\infty}^{\infty} \delta\mathbf{u}_{c(m)} e^{j2\pi m t/T}\right] \tag{A4}$$

from which the Fourier coefficient vector $\mathbf{u}_{c0}+\delta\mathbf{u}_{c(0)}$ with the maximum vector norm and thus the integer k can be easily identified.
(3) Determine the basis set of μ and $\mathbf{u}_c(t)$ from the relations

$$\mu = \mu' + j\frac{2\pi k t}{T}, \quad \mathbf{u}_c(t) = \mathbf{u}_c'(t)e^{-j2\pi k t/T} \tag{A5}$$

The Poincare exponents that are determined from the above procedure are called the eigenvalues belonging to cluster 0 [6], i.e.,

$$\mu_r^i = \lambda_{r(0)}^i, \quad r = \pm 1, \pm 2, \ldots, \pm N, \quad i = B,F$$

The above procedure is consistent with the order analysis of vector norm summarized in Table 1, because it holds

$$\|\mathbf{u}_{c0} + \delta\mathbf{u}_{c(0)}\| = \max\{\|\mathbf{u}_0 + \delta\mathbf{u}_{(0)}\|, \|\hat{\mathbf{u}}_0 + \delta\hat{\mathbf{u}}_{(0)}\|\}$$
$$\sim \max\{O(1), O(\Delta)\} = O(1)$$

Here, the norm of the Fourier coefficient vectors, except $m=0$, is of order equal to or higher than δ. The above procedure excludes the special case of an asymmetric rotor system, which can be formulated as a time-invariant linear system in the rotating coordinates.

Appendix B: Computational Efficiency With $\mathbf{L}(\omega,\Omega)$ and $\hat{\mathbf{L}}(\omega,\Omega)$

The size of system matrices in Eq. (1) is $N\times N$, N being the number of complex coordinates required to describe the system dynamic behavior. Now assume that the rotational speed is fixed at $\Omega=\Omega_1$. For every rotational speed of interest, the approximate eigenvalue problem with fair accuracy can be formulated from the $12N\times 12N$ Hill's reduced order matrix [6]. Then the four $N\times N$ dFRMs can be derived as given in Eq. (19). Construction of $N\times N$ residue matrices at n_m modes of interest for each dFRM requires $n_m N^2$ multiply operation. For $N\times N$ residue matrices given at n_m modes of interest, calculation of each $N\times N$ dFRM at n_ω spectral lines and its infinity norm requires $n_m n_\omega N^2$ divide-add operation. The speed ratio, r_L, in computation of $\hat{L}_{ik}(\omega,\Omega_1)$ to $L_{ik}(\omega,\Omega_1)$, $i,k=1,2$, then becomes N^2, because computation of each $\hat{L}_{ik}(\omega,\Omega_1)$ takes $n_m n_\omega$ divide-add operation. For the commercial generator treated in Sec. 4.3, $N=42$, $n_m=84$, and $n_\omega=2000$ were used to compute dFRMs, resulting in $r_L=N^2\sim 1600$. Note that the computational time needed for $L_{ik}(\omega,\Omega_1)$ increases rapidly in proportion to N^2, while the computational time for $\hat{L}_{ik}(\omega,\Omega_1)$ is almost independent of N. Besides the computational burden, another critical problem with direct computation of $L_{ik}(\omega,\Omega_1)$ is the memory shortage as N increases, because the size of data storage required in the computational process of $L_{ik}(\omega,\Omega_1)$ is $n_\omega N^2$, whereas $\hat{L}_{ik}(\omega,\Omega_1)$ takes only n_ω memory space.

Appendix C: Equation of Motion for the Anisotropic Rigid Rotor (Sec. 2.8 of Ref. [3])

The equation of motion for the anisotropic rigid rotor in Fig. 2 can be written, in the complex coordinates, as

$$\begin{bmatrix} m\ell_2^2 + i_T & m\ell_1\ell_2 - i_T \\ m\ell_1\ell_2 - i_T & m\ell_1^2 + i_T \end{bmatrix}\begin{Bmatrix} \ddot{p}_1(t) \\ \ddot{p}_2(t) \end{Bmatrix} + \begin{bmatrix} -ji_p\Omega & ji_p\Omega \\ ji_p\Omega & -ji_p\Omega \end{bmatrix}\begin{Bmatrix} \dot{p}_1(t) \\ \dot{p}_2(t) \end{Bmatrix}$$
$$+ \begin{bmatrix} k & 0 \\ 0 & k \end{bmatrix}\begin{Bmatrix} p_1(t) \\ p_2(t) \end{Bmatrix} + \begin{bmatrix} \Delta k & 0 \\ 0 & \Delta k \end{bmatrix}\begin{Bmatrix} \bar{p}_1(t) \\ \bar{p}_2(t) \end{Bmatrix} = \begin{Bmatrix} g_1(t) \\ g_2(t) \end{Bmatrix} \tag{C1}$$

where $i_T=J_T/L^2, i_p=J_p/L^2$, $\ell_1=L_1/L, \ell_2=L_2/L$, and $L_1+L_2=L$. Here, the subscripts 1 and 2 represent the bearing location; m, J_T, and J_p are the mass, transverse, and polar mass moments of inertia about the center of gravity of the rotor, respectively; L_1 and L_2 are the distance of the bearings from the center of gravity; and k and Δk are the mean and deviatoric stiffnesses of bearings, implying that the stiffnesses of each bearing are $k+\Delta k$ and $k-\Delta k$ in the y and z directions, respectively. The simulation data are taken as $m=1, k=0.5, \Delta k=0.04$, $\ell_1=0.25, \ell_2=0.75$, and $i_T=0.0625, i_p=0.5i_T$, as the rotational speed Ω was varied up to 4. To prevent the blowup of dFRFs and FRFs at resonances, as a matter of graphical convenience, the real part of all eigenvalues was set to be 0.01.

Appendix D: Practicality of Smallness in Anisotropy and Asymmetry [3]

For a general rotor system, the dynamic stiffness matrix associated with the anisotropic (asymmetric) element coordinates can be reduced to

$$\mathbf{D}_\Omega(j\omega) = -\omega^2\mathbf{M}(\Omega) + j\omega\mathbf{C}(\Omega) + \mathbf{K}(\Omega) \tag{D1}$$

The nonsymmetric, in general, dynamic stiffness matrix can be decomposed into a symmetric and a skew-symmetric matrix as

$$\mathbf{D}_\Omega(j\omega) = \begin{bmatrix} \mathbf{D}_{yy} & \mathbf{D}_{yz} \\ \mathbf{D}_{zy} & \mathbf{D}_{zz} \end{bmatrix} = \begin{bmatrix} \mathbf{D}_{yy} & \mathbf{D}_a \\ \mathbf{D}_a & \mathbf{D}_{zz} \end{bmatrix} + \begin{bmatrix} \mathbf{0} & \mathbf{D}_s \\ -\mathbf{D}_s & \mathbf{0} \end{bmatrix} \tag{D2}$$

Introducing a proper rotation matrix, we can always transform the above expression to

$$\mathbf{D}^*_{\Omega}(j\omega) = \mathbf{R}\mathbf{D}_{\Omega}(j\omega)\mathbf{R}^T = \begin{bmatrix} \mathbf{D}^*_{yy} & \mathbf{D}_s \\ -\mathbf{D}_s & \mathbf{D}^*_{zz} \end{bmatrix} \tag{D3}$$

Thus the smallness, Δ, of anisotropy (asymmetry) can be defined as

$$\Delta = \frac{\left|\|\mathbf{D}^*_{yy}\| - \|\mathbf{D}^*_{zz}\|\right|}{\|\mathbf{D}^*_{yy}\| + \|\mathbf{D}^*_{zz}\|} < \frac{\|\mathbf{D}_s\|}{\|\mathbf{D}^*_{yy}\| + \|\mathbf{D}^*_{zz}\|} \tag{D4}$$

Note that $\|\mathbf{D}_s\|$, which includes the gyroscopic moment effect, grows much faster than $\|\mathbf{D}^*_{yy}\|+\|\mathbf{D}^*_{zz}\|$, representing the mean stiffness of the system, as the rotational speed increases. Thus, the above smallness assumption is valid for most practical rotors.

References

[1] Lee, C. W., and Joh, C. Y., 1994, "Development of the Use of the Directional Frequency Response Functions for the Diagnosis of Anisotropy and Asymmetry in Rotating Machinery: Theory," Mech. Syst. Signal Process., **8**(6), pp. 665–678.

[2] Lee, C. W., and Lee, S. K., 1997, "An Efficient Complex Modal Testing Theory for Asymmetric Rotor Systems: Use of Unidirectional Excitation Method," J. Sound Vib., **206**(3), pp. 327–338.

[3] Lee, C. W., 1993, *Vibration Analysis of Rotors*, Kluwer Academic, Dordrecht.

[4] Bucher, I., and Ewins, D. J., 2000, "Modal Analysis and Testing of Rotating Structures," Philos. Trans. R. Soc. London, Ser. A, **359**, pp. 61–96.

[5] Nordmann, R., 1984, "Identification of Modal Parameters of an Elastic Rotor With Oil Film Bearings," ASME J. Vib., Acoust., Stress, Reliab. Des., **106**, pp. 107–112.

[6] Lee, C. W., Han, D. J., Suh, J. H., and Hong, S. W., 2007, "Modal Analysis of Periodically Time-Varying Linear Rotor Systems," J. Sound Vib., **303**, pp. 553–574.

[7] Suh, J. H., Hong, S. W., and Lee, C. W., 2005, "Modal Analysis of Asymmetric Rotor System With Isotropic Stator Using Modulated Coordinates," J. Sound Vib., **284**, pp. 651–671.

[8] Campbell, W. E., 1924, "The Protection of Steam Turbine Disk Wheels From Axial Vibration," Trans. ASME, **46**, pp. 31–160.

[9] Crandall, S. H., 1995, "Rotordynamics," *Nonlinear Dynamics and Stochastic Mechanics*, W. Kliemann and N. S. Namachchivaya, eds., CRC, Boca Raton, FL.

[10] Dimentberg, F. M., 1961, *Flexural Vibrations of Rotating Shafts*, Butterworths, London.

[11] Rao, J. S., 1991, *Turbomachine Blade Vibration*, Wiley Eastern, New Delhi.

[12] Irretier, H., 1988, "Free and Force Vibrations of Turbine Blades," *Rotordynamics 2: Problems in Turbomachinery*, N. F. Rieger, ed., Springer-Verlag, Berlin.

[13] Lalanne, M., and Ferraris, G., 1990, *Rotordynamics Prediction in Engineering*, Wiley, New York.

[14] Nelson, H. D., and Crandall, S. H., 1992, "Analytic Prediction of Rotordynamic Response," *Handbook of Rotordynamics*, F. F. Ehrich, ed., McGraw-Hill, New York.

[15] Singh, M. P., 1984, "SAFE," Dresser-Rand Company Technology Report No. ST 16.

[16] Lancaster, P., 1966, *Lambda-Matrices and Vibrating Systems*, Pergamon, New York.

[17] Lee, C. W., and Han, D. J., 2008, "Strength of Modes in Rotating Machinery," J. Sound Vib., **313**, pp. 268–289.

[18] Lee, C. W., 2005, "Evolution of Campbell Diagram With Modal Strength in Rotating Machinery," 11th Asia Pacific Vibration Conference, Malaysia.

[19] Lee, C. W., 1991, "A Complex Modal Testing Theory for Rotating Machinery," Mech. Syst. Signal Process., **5**, pp. 119–137.

[20] Genta, B., 1988, "Whirling of Unsymmetrical Rotors: A Finite Element Approach Based on Complex Coordinates," J. Sound Vib., **124**, pp. 27–53.

[21] Ardayfio, D., and Frohrib, D. A., 1976, "Instability of an Asymmetric Rotor With Asymmetric Shaft Mounted on Symmetric Elastic Supports," ASME J. Eng. Ind., **98**, pp. 1161–1165.

[22] Lancaster, P., and Tismenetsky, M., 1985, *The Theory of Matrices With Application*, 2nd ed., Academic, New York.

[23] Calico, R. A., and Wiesel, W. E., 1984, "Control of Time-Period Systems," J. Guid. Control Dyn., **7**, pp. 671–676.

[24] Gourlay, A. R., and Watson, G. A., 1973, *Computational Methods for Matrix Eigenproblems*, Wiley, New York.

[25] Bently, D. E., 2002, *Fundamentals of Rotating Machinery Diagnostics*, Bently Pressurized Bearing Press, Minden.